JOURNAL OF CATALYSIS 128, 218–230 (1991)

Reduction/Oxidation of a High Loading Iron Oxide Catalyst

HEON JUNG AND WILLIAM J. THOMSON

Department of Chemical Engineering, Washington State University, Pullman, Washington 99164-2710

Received August 3, 1990; revised September 18, 1990

The reduction/oxidation of a high loading iron catalyst supported on γ-Al_2O_3 has been studied using dynamic X-ray diffraction (DXRD). *In situ* determination of changes in the lattice parameters as magnetite was reduced to iron indicated that aluminum was unevenly incorporated into the matrix of the supported iron oxide particles, leading to a form of metal–support interaction and manifested by reduction rates which are much slower than for unsupported magnetite. These results are corroborated in subsequent oxidation experiments by the fact that CO_2 oxidation rates of supported iron are much higher than for unsupported iron and the Fe_2O_3 phase formed in the former at 673 K is γ-Fe_2O_3 as opposed to α-Fe_2O_3 in the latter. The rate data are modeled and the results are shown to be consistent with the conclusion of nonuniform Al incorporation as well as with previous work on the oxidation of unsupported iron. The incorporation of Al in this Fe/Al_2O_3 catalyst is consistent with previous observations related to the form of metal–support interactions in Ni/Al_2O_3 and in Fe/SiO_2.

INTRODUCTION

In most cases the activation of metal catalysts consists in a reduction of metal oxides by gaseous reducing agents, and this has been the focus of a great deal of research (*1*). We report here on the reduction of iron catalysts, which are extensively used in important industrial processes such as ammonia synthesis, Fischer–Tropsch synthesis, and water gas shift reaction, and are either unsupported or supported on a carrier.

Unsupported iron catalysts are primarily composed of iron and of small concentrations of promoters. Studies of the reduction of unsupported iron catalysts have been largely confined either to the kinetics of the reduction, i.e., reduction mechanisms (*2–5*), or to the characterization of promoters (*6, 7*). In general the reduction behavior of unsupported iron catalysts is adequately modeled by a shell and core model, which has been well accepted in pure hematite (α-Fe_2O_3) reduction studies (*8–11*). Topsøe *et al.* (*6*) studied the reduction behavior of a singly promoted iron catalyst with a homogeneous distribution of Al_2O_3 and proposed the formation of $FeAl_2O_4$ inclusions in iron during the initial stages of reduction and Al_2O_3 inclusions during the final stages. Although they dealt with an unsupported catalyst, their results lend insight to metal–support interactions of iron catalysts supported on alumina carriers.

Studies of the reduction of supported iron catalysts have largely focused on characterization issues rather than on kinetics, simply because of the complexity of the reduction of supported iron oxide. On the other hand, reducibility has been a generally useful means for detecting interactions between the metal and the support material in supported catalytic systems (*12*). The complexity of supported iron reduction is illustrated by the fact that, when the loading of iron on alumina is as low as 0.05%, Fe^{+3} reduces only to Fe^{+2} even at temperatures as high as 973 K in hydrogen (*13*). In contrast, unsupported iron oxide can be reduced to the zero-valent state at 673 K (*6*). The inferior reducibility of supported iron catalysts is currently thought to be due to the stabilization of ferrous cations by the interaction with support oxygen anions; i.e., by the for-

0021-9517/91 $3.00

mation of surface compounds with the support, such as surface spinel (*14*). For example, an *in situ* TPR–Mössbauer spectroscopy study of Fe/Al_2O_3 revealed the formation of iron aluminate ($FeAl_2O_4$) during reduction (*15*). Also, Sushumna and Ruckenstein (*16*) used TEM and electron diffraction on a "model" Fe/Al_2O_3 catalyst and showed the formation of solid solutions or aluminates as a form of the chemical interaction between iron oxide and alumina supports. However, it is not certain whether the solid solutions are formed during the preparation of the catalyst or during the reduction, or both. An *in situ* reduction and characterization technique is ideally suited to unravel questions of this nature.

Mössbauer spectroscopy is a powerful characterizing tool for catalysts containing iron, but the identification of specific chemical compounds, such as spinel species, is difficult (*16, 17*). Furthermore, since it is difficult to obtain meaningful spectra at relatively high reaction temperatures using *in situ* Mössbauer spectroscopy, spectra are usually collected at either room temperature or lower (*1*). In that case *in situ* Mössbauer spectroscopy is basically a "quench and analyze" technique which is both tedious and limited to relatively slow reactions.

X-ray diffraction (XRD) can be a complementary technique to determine phase specific compounds in solids and the accurate determination of lattice parameters makes it possible to determine the composition of solid solutions as well as to identify pure compounds (*18*). The use of *in situ* XRD has already demonstrated the feasibility of its use in catalysis research (*19, 20*). The recent addition of a dynamic capability, dynamic X-ray diffraction (DXRD) (*21, 22*), also makes it possible to follow the *in situ* reduction behavior of supported oxides in a phase-specific manner. This can be done both qualitatively and quantitatively via the identification of reduction paths and the determination of the extent of reaction without interrupting the reduction procedure. The quantifying ability of DXRD makes it a substitutional or complementary technique for thermogravimetric analysis (TGA). Moreover, DXRD can overcome some of the difficulties encountered in TGA experiments such as the differentiation between mass changes associated with reduction/oxidation vs. those related to adsorption/desorption or even dehydration, and the inability of TGA to distinguish between phases at each stage of the reaction when several intermediate phases are present (*1*).

In situ DXRD has been used in this study to investigate the reduction/oxidation behavior and kinetics of a high loading Fe/Al_2O_3 catalyst in an attempt to corroborate previous hypotheses relative to the difficulty of reducing such catalysts. In particular, the results are interpreted in terms of the chemical interactions between iron and the support. The reduction of unsupported iron oxide was also studied in a similar manner in order to provide a basis of comparison with the reduction of supported iron oxides.

EXPERIMENTAL

Materials

The catalyst used in this study is a high loading iron catalyst supported on a high surface area γ-Al_2O_3 (Norton Co.; BET area 224 m^2/g, pore volume 0.631 cm^3/g). The catalyst was prepared by successive impregnations of solutions of $Fe(NO_3)_3 \cdot 9H_2O$ (Mallincrodt) until a loading of 31.8 wt% of iron was achieved. After the support particles (100–200 mesh) were wetted with the solution, the catalyst was dried at 383 K for 24 h and then calcined at 673 K in air for 24 h. This cycle was repeated six times. Studies were also conducted with bulk, unsupported hematite (α-Fe_2O_3, J T Baker) as well as with a commercial, chromia promoted magnetite (Katalco, 10% Cr_2O_3, 0.4% CrO_3), the former to provide a basis of comparison with respect to reduction and the latter for purposes of comparing the water gas shift (WGS) reaction activity of the supported magnetite catalyst. The properties of all

TABLE 1

Physical Properties of Fresh and Reduced Materials Tested

	Fe_2O_3/Al_2O_3	Unsupported	Promoted
Percent Fe_2O_3 (by weight)	40.0	100	85
Total surface area (fresh, m^2/g cat)	81.25	11.74	140.5
Total surface area (reduced, m^2/g cat)	91.99	—	5.91
Metal surface area (m^2/g iron)	90.5	7.4	10.4
Pore volume (fresh, cm^3/g cat)	0.232	0.244	0.219
Fe_2O_3 crystallite size (Å, by XRD)	178	<1000	—
Fe crystallite size (Å) (by CO chemisorption)	84	1037	733

three materials are listed in Table 1. Gases used in this study were high purity grade and were used as is, except for hydrogen, which first passed through a deoxo unit and then a molecular sieve trap.

DXRD

Figure 1 shows a schematic of the DXRD equipment configuration. The specific details of the DXRD equipment have been given elsewhere (*21, 22*), but it consists of a Siemens D500 θ-2θ powder diffractometer equipped with a flow-through, Anton–Paar hot stage and a position sensitive detector capable of rapid scanning (60°/min) at high resolution (0.01°). Because of fluorescence problems with iron catalysts, Co$K\alpha$ radiation and an iron filter were used in all of the experiments reported here. A thin (less than 0.3 mm) sample of powdered catalyst (20–150 μm) was placed on a platinum strip which was electrically heated. A type S thermocouple, attached to the strip, served as a temperature monitor and was used to control the temperature or heating program by means of Micristar Model 828D controller. Tracer tests of the hot stage reaction chamber indicate that, at the gas flows used here (300–2500 ml/min), it behaves similarly to a perfect back-mixed reactor.

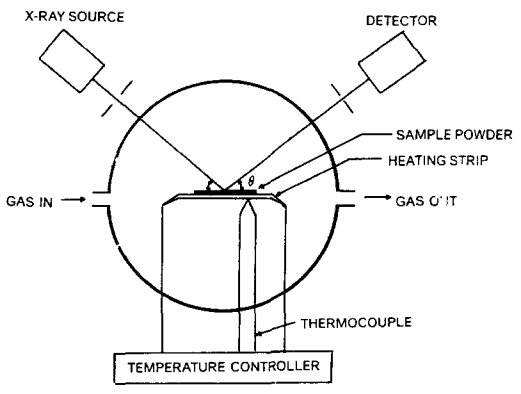

FIG. 1. Schematic diagram of DXRD reaction chamber.

Procedures

Reduction and oxidation experiments were carried out at 100 kPa with supported and unsupported iron or iron oxide using H_2 and CO_2, respectively. Temperatures were varied between 573 and 673 K and the gas flowrates were about 1500 ml/min, sufficient to eliminate gas–solid mass transfer effects. DXRD scans were performed at appropriate time intervals during the run and quantitative analysis of the DXRD data was accomplished by using the "External Standard Method" (*18, 23*) to determine the weight fractions of each phase (hematite (α-Fe_2O_3), magnetite (Fe_3O_4), and iron (Fe)). The degree of reduction (ratio of quantity of oxygen removed to quantity of oxygen removable from the initial oxide), R, was calculated from the mass fractions of the observed species. To determine the composition of

solid solutions (between FeO and Al_2O_3 or between Fe_3O_4 and γ-Fe_2O_3), lattice parameters were accurately measured. The centroid of the peak in question, $C(2\theta)$, was determined by numerically evaluating

$$C(2\theta) = \frac{\int (2\theta)\, I(2\theta)\, d(2\theta)}{\int I(2\theta)\, d(2\theta)},$$

where $I(2\theta)$ is the intensity of the diffracted X-ray (*24*). With $C(2\theta)$ determined, the lattice parameter of the cubic cell can be calculated by the equation

$$a = \frac{\lambda \times \sqrt{h^2 + k^2 + l^2}}{2 \sin (C(2\theta)/2)},$$

where "a" is the lattice parameter, λ is the radiation wave length, and $C(2\theta)$ is the centroid of the (hkl) peak. In order to insure reliability and repeatability, the angular shift due to strip misalignment was corrected by an internal molybdenum standard which was mixed with the sample. Mo was chosen as the standard because its primary diffraction peak is close to that of magnetite and there is no peak overlap. Alloy formation between iron and Mo was not observed during any of the experiments conducted here. Average particle sizes were calculated using Scherrer's formula with Warren's correction (*24*).

Reduced samples were also subjected to CO chemisorption measurements using a pulse technique (Flowsorb II, Micromeritics). The total adsorption (chemisorption and physical adsorption) of CO was measured at 77.7 K and the amount of physical adsorption was determined by measuring the amount of desorbed CO when the sample temperature was raised to 195 K. The difference between the two gives the chemisorbed amount of CO. Reduced iron surface areas determined by CO chemisorption (area occupied by a CO molecule on Fe surface assumed to be 12 Å) and the average particle sizes calculated from the chemisorption measurements are also listed in Table 1. The water gas shift reaction activity measurements were performed in a continuous flow reactor with on-line GC. The experiments were carried out at atmospheric pressure and at a temperature of 773 K with H_2O/CO ratio of 2.7 (partial pressure of CO 27 kPa). The activity was expressed as the rate of conversion of carbon monoxide to carbon dioxide per gram of Fe_3O_4.

RESULTS AND DISCUSSIONS

The water gas shift (WGS) reaction activity of the supported magnetite was about one fourth of the activity of the chromia promoted magnetite catalyst (Fig. 2). Because the active form of the catalyst used in the WGS reaction is Fe_3O_4 (oxide), the catalytically active surface area of the Fe_3O_4 by chemisorption is not known. If the activities are compared on the basis of iron area, then the turnover frequency of the supported catalyst is an order of magnitude less than that of the chromia promoted catalyst. On the other hand, the supported catalyst exhibited superior sintering stability during the reduction to iron, whereas the BET area of the promoted catalyst dropped by an order of magnitude when reduced to iron.

The supported iron oxide was scanned by XRD after the calcination step and was found to be in the form of α-Fe_2O_3 (hematite). However, there were noticeable shifts in the positions of the supported hematite peaks when compared to those of unsupported hematites. The shifts result from changes in the cell dimension of the supported hematite; that is, the lattice parameters of the supported hematite on γ-Al_2O_3 were smaller. Similar observations were made by Rooksby (*25*) for unsupported hematite formed from goethite (α-FeOOH), in which Al replaces some of the iron and has small cell dimensions than the corresponding material produced from Al-free goethite. The smaller cell dimensions of supported hematite indicate that some of the aluminum is incorporated in the disordered hematite structure. During the impregnation procedure it is likely that some of the Al in γ-Al_2O_3 was dissolved in the acidic iron nitrate solution and this dissolved Al is thought to be

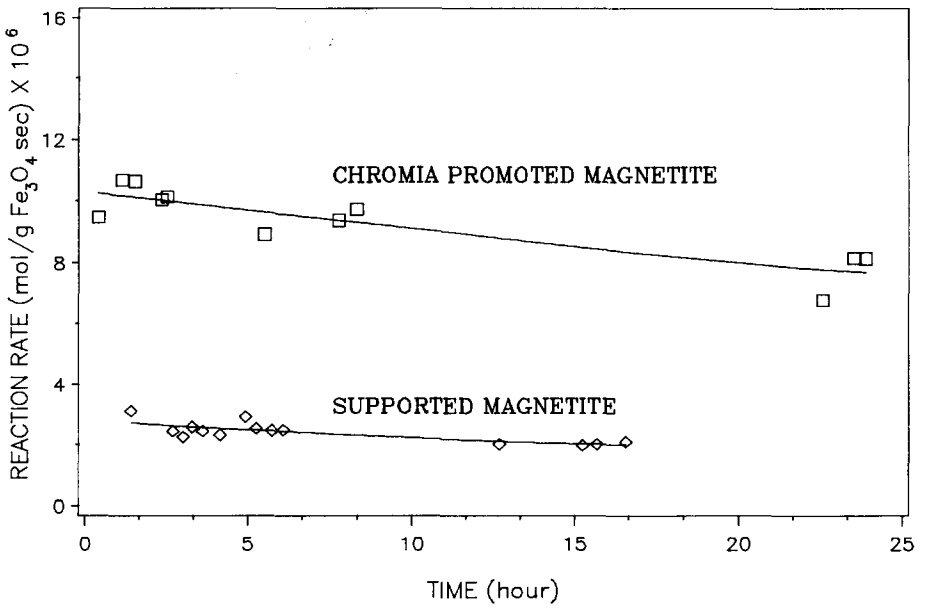

FIG. 2. Water gas shift reaction activity (T = 773 K, P_{H_2O}/P_{CO} = 2.7).

incorporated into the matrix of the hematite upon crystallization and calcination. This was verified by Vaishinava *et al.* who studied Fe/Al_2O_3 by Mössbauer spectroscopy and found that the calcined Fe/Al_2O_3 was composed of Fe^{3+} ions strongly interacting with the alumina surface to form a solid phase containing Fe, Al, and O, and 10% bulk hematite (*26*).

Reduction

The reduction of hematite at temperatures below 843 K is known to proceed in a stepwise manner:

$$\alpha\text{-}Fe_2O_3 \rightarrow Fe_3O_4 \rightarrow Fe.$$

This reduction sequence is clearly seen in Fig. 3, which shows the DXRD spectra of the supported hematite in a hydrogen stream at 673 K. As can be seen, it is only after the complete reduction of hematite (α-Fe_2O_3) to magnetite (Fe_3O_4) that magnetite is further reduced to iron. The advantage of DXRD over TGA is evident, since DXRD tracks the changes in the specific phases during the reduction as well as the total degree of reduction. The ability of DXRD to provide accurate quantitative data was confirmed by comparing XRD results with TGA results, as shown in Fig. 4. In this set of experiments, unsupported hematite samples were run on a TGA to a particular degree of reduction and then subjected to quantitative XRD analysis. As can be seen the data agree very well. In addition, three identical reduction runs were conducted using DXRD and the degree of reduction data was repeatable within 5% or less.

A comparison of the reduction rates of the supported and unsupported hematites at 673 K is shown in Fig. 5. The reduction rate of the supported iron oxide was much lower than that of the unsupported samples, indicating metal–support interactions of the γ-Al_2O_3 supported iron oxide. In previous work with alumina promoted iron catalysts for ammonia synthesis, the reduction rate was found to decrease with an increase in the concentration of alumina (*5*). Since the supported iron oxide in this work contains aluminum in the matrix of the hematite, it is likely that the incorporated aluminum can

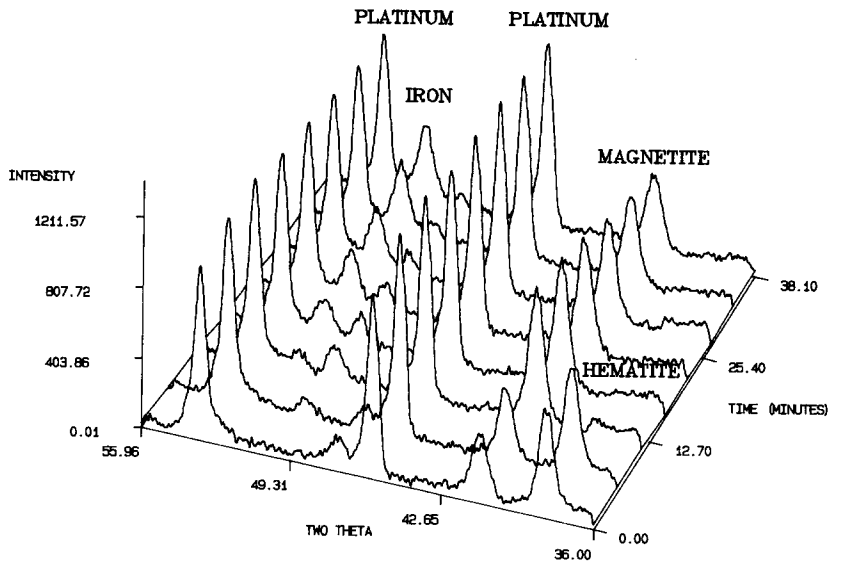

FIG. 3. DXRD reduction data for supported iron oxide (T = 673 K, P_{H_2} = 100 kPa).

retard the reduction of supported iron catalysts in a similar manner as the alumina in promoted iron catalysts.

The cubic cell lattice parameter of the solid solution of Al_2O_3 in Fe_3O_4 is known to decrease linearly with increasing content of Al, obeying Vegard's law (*27*). Therefore, an accurate determination of the lattice parameter of the solid solution of Al_2O_3 in Fe_3O_4 can be used to determine the content

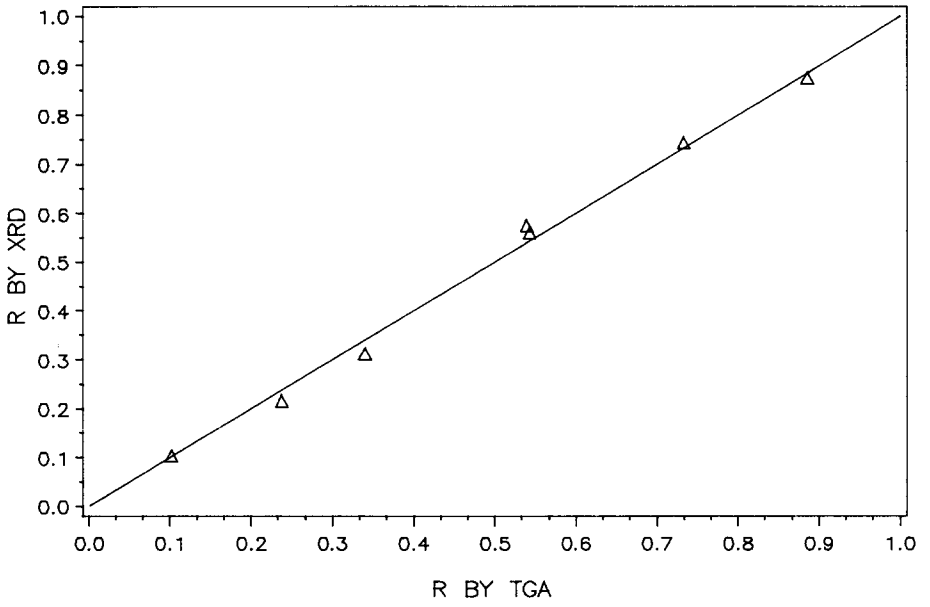

FIG. 4. Comparison of TGA and XRD reduction data (T = 673 K, P_{H_2} = 100 kPa).

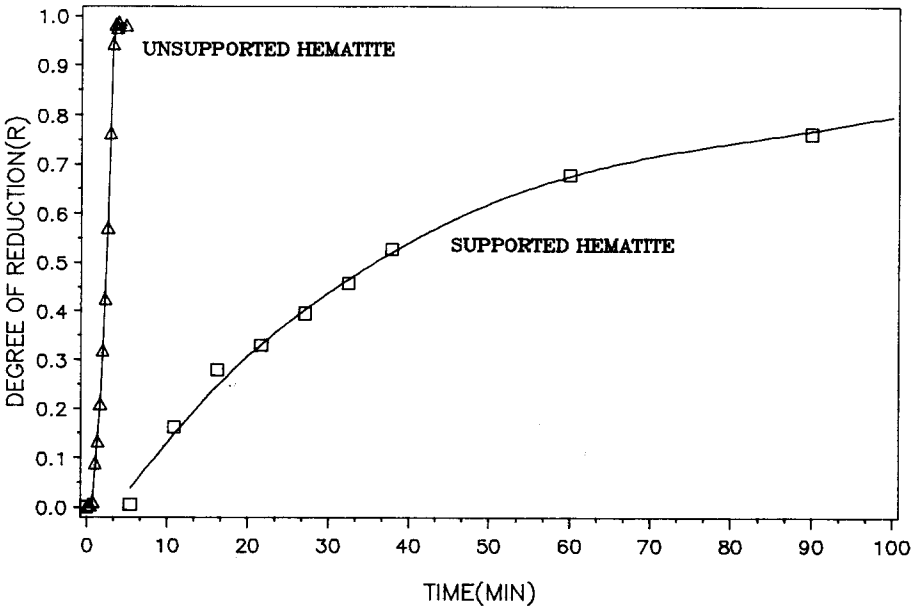

FIG. 5. Hematite reduction rates (T = 673 K, P_{H_2} = 100 kPa).

of Al in the solid solution, using the known lattice parameters of Fe_3O_4 (8.402 Å) and $FeAl_2O_4$ (8.15 Å). After the reduction of supported hematite to the magnetite state, the lattice parameter was measured by XRD and the Al in the supported solid solution was found to be 9.0 at%. The change in the lattice parameter of the Fe_3O_4–Al solid solution was then continuously monitored during the reduction of magnetite to iron at 673 K, and the results are shown in Fig. 6. As can be seen, the lattice parameter decreases as the reduction of magnetite proceeds, indicating that, as the reduction proceeds, the remaining unreduced solid solution becomes richer in Al concentrations. The process follows the reaction

$$Fe_{3-x}Al_xO_4 + \frac{4y}{x+y}H_2 \rightarrow \frac{x}{x+y}Fe_{3-x-y}Al_{x+y}O_4 + \frac{3y}{x+y}Fe + \frac{4y}{x+y}H_2O.$$

The incorporated Al can be distributed in the supported iron oxide particles in a homogeneous manner, as in alumina-promoted iron catalysts, or in an uneven or localized distribution. If the Al is locally distributed, there will be high Al content near the interface of the metal and the support surface, and low Al content far from the interface. Considering the high metal loading (40 wt% of Fe_2O_3), an uneven distribution of Al in the iron oxide is more likely. If Al in the supported iron oxide is evenly distributed, the XRD peaks of the solid solution will shift toward $FeAl_2O_4$ as well as decreasing in size. This decrease would be due to the disappearance of Fe_3O_4 and the peak shift would result from the fact that the remaining solid solution would be higher in Al concentration. Schematically, the XRD peaks in this reduction process will probably undergo the change depicted in Fig. 7 (a), where each peak represents the peak of homogeneous solid solution of magnetite with a different aluminum concentration. In this case the XRD peak height of the solid solution will decrease linearly with the shift of the peak position, which is shown as a solid line in Fig. 7 (b). However, when the actual supported Fe_3O_4–Al catalyst was reduced,

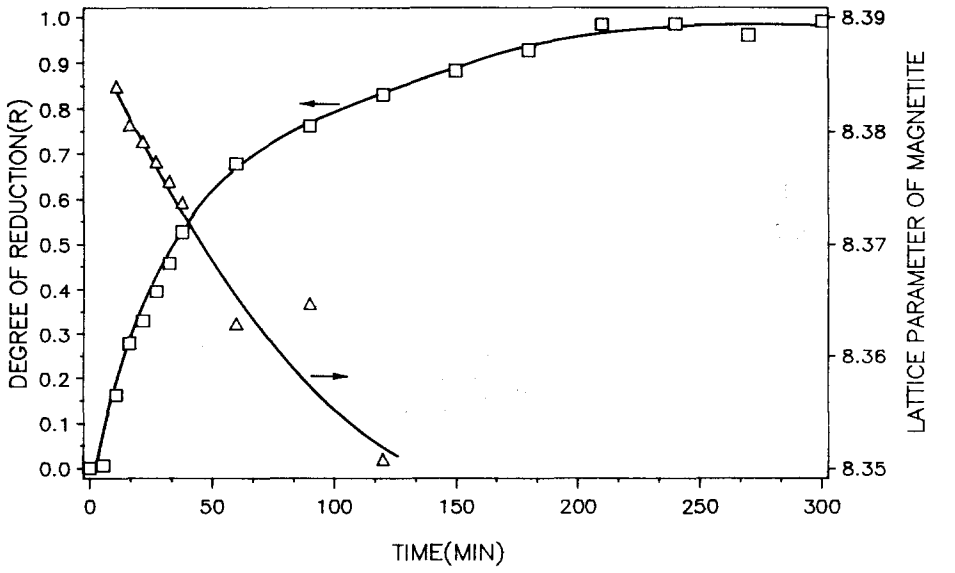

FIG. 6. Degree of reduction and lattice parameters during reduction (supported hematite, T = 673 K, P_{H_2} = 100 kPa).

the XRD peak changed in a nonlinear fashion as evidenced by the data points in Fig. 7 (b). Thus, during the early stage of reduction of the supported magnetite, the XRD peak shift was not as pronounced as it should have been if Al had been evenly distributed. This suggests that the initial solid solution peak is the convolution of two peaks; one is the peak corresponding to high Al content solid solutions and the other is that of low Al content solid solutions. The solid solutions with lower Al content will be reduced dominantly at the initial stage of the reduction and the solutions with higher Al content will be reduced later, since solid solutions high in Al content are not easily reducible. Consequently, the XRD peak corresponding to low Al content solid solution will decrease with small changes in its centroid location and this will occur early in the reduction process. In the latter stage of reduction, the high Al content solid solutions will be reduced, resulting in large changes in peak position since even small extents of reduction here will lead to large changes in the concentration of Al in the remaining solid solution. This explanation is consistent with the data in Fig. 7 (b). Similar phenomena have also been previously observed with other supported catalysts. For example, Boudart *et al.* (*28*) also observed the formation of solid solutions of FeO–MgO for Fe/MgO catalysts after reduction. In fact, Lund and Dumesic showed that when Fe_3O_4 is supported on SiO_2, a strong oxide–oxide interaction was observed, resulting from the substitution of Si^{+4} for Fe^{+3} at the tetrahedrally coordinated cation sites of Fe_3O_4 (*29*). Similarly, Lo Jacono *et al.* (*30*) and Dufresne *et al.* (*31*) found that the surface spinal of $NiAl_2O_4$ was formed in Ni/Al_2O_3 systems and, in an investigation of a coprecipitated Ni/SiO_2 catalyst, Shalvoy *et al.* (*32*) concluded that the fresh (unreduced) catalysts were composed of amorphous $NiSiO_2$, easily accessible NiO, and relatively inaccessible NiO. Their conclusion supports our result of two types of supported iron oxide: oxides strongly interacting with the support by

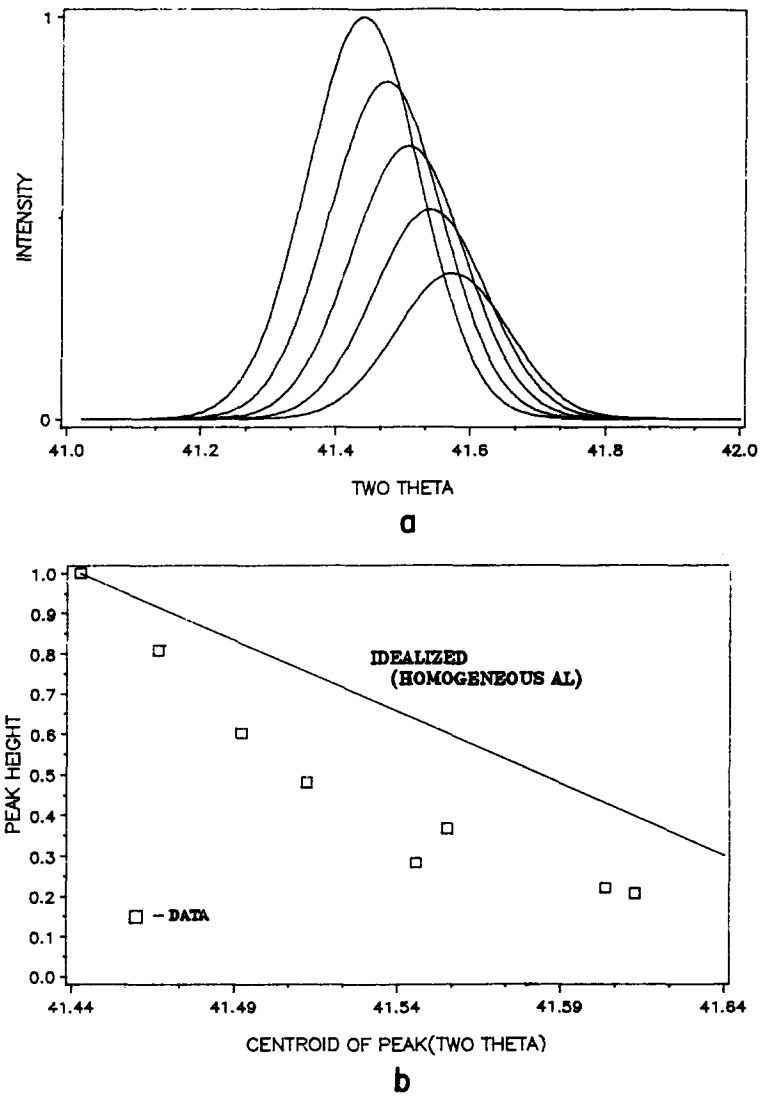

FIG. 7. (a) Idealized XRD patterns for reduction of iron oxide with homogeneous aluminum incorporation; (b) Peak height vs. peak centroid during reduction: idealized vs. actual data.

forming solid solutions with it, and oxides which do not interact with the support as strongly.

Given that the experimental evidence supports a localized incorporation of aluminum in the supported iron oxide, the unreacted shrinking core model with interface reaction control (*8*) was applied to the quantitative reduction data. The fit to the data at 673 K is shown in Fig. 8, where R is the degree of the reduction. Although the data for the entire reduction process, from hematite to iron, are shown here, it should be pointed out that hematite converts completely to magnetite at $R = 0.11$. So, in effect, the kinetic fit corresponds to the reduction of magnetite to iron. The fact that two straight lines with different slopes are

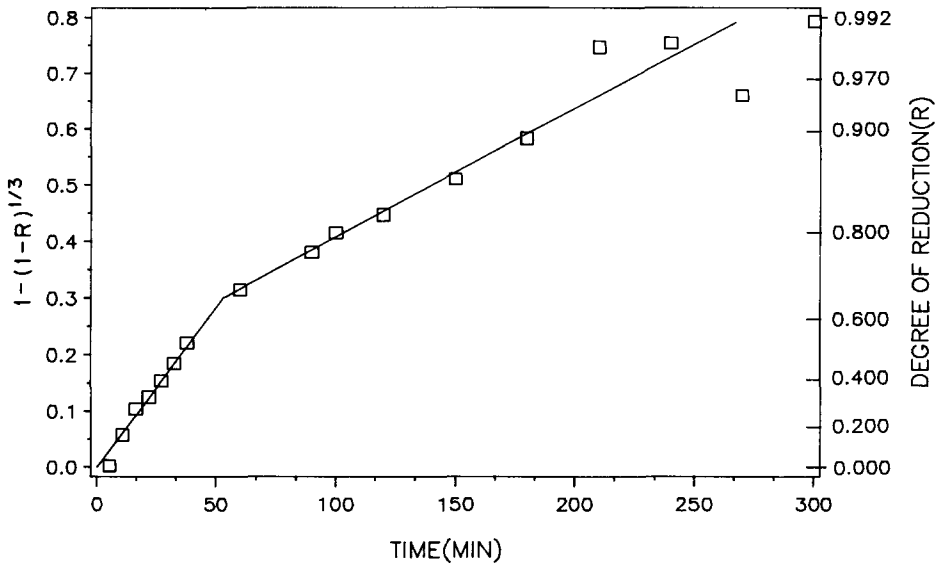

FIG. 8. Fit of reduction data to interface reaction-controlled shrinking core model (supported hematite, T = 673 K, P_{H_2} = 100 kPa).

needed to fit the data means that there is a change is the reaction rate at the interface at about $R = 0.7$. The first line in Fig. 8 could be interpreted to represent the reduction of solid solutions with low Al concentration and the second line to represent that of Al-rich solid solutions. The difference in the reducibility of each material is believed to cause the slope change. If, on the other hand, deviations from one straight line are due to changes in the reduction mechanism, the deviation would be expected to be continuous, rather than to make another distinct straight line (*9, 33*). Thus all the data are consistent with a localized Al distribution in the supported iron oxide particles, resulting in two distinct reduction steps, the first being the Al-difficient solid solutions and the second the reduction of Al-rich solutions. It should be also pointed out that the DXRD reduction data of unsupported magnetite to iron were also successfully fit to an unreacted shrinking core model with magnetite/iron interface reaction control, which is consistent with previous observations (*8, 10, 11*).

Oxidation

DXRD spectra of the CO_2 oxidation of the iron produced by the reduction of unsupported hematite are shown in Fig. 9 at 673 K. The coexistence of iron, magnetite, and hematite is observed after 180 min of oxidation, pointing to the presence of multilayered oxidation on individual iron particles. This was not observed in the oxidation of the supported iron; that is, iron was completely oxidized to magnetite prior to further oxidation which, in this case, resulted in the formation of maghemite (γ-Fe_2O_3). This is due to vastly different particle sizes in the two systems (see Table 1). Previous work on the oxidation of iron at low temperatures ($T <$ 843 K) also exhibited multilayered scales such as Fe_2O_3 and Fe_3O_4 (*34*). A comparison of the oxidation rate curves at 673 K for both materials is shown in Fig. 10 . In this case, the supported iron had much higher oxidation rates than the unsupported samples. The temperature programmed oxidation (TPO) results of Kadkhodayan and Brenner (*35*) also showed that the oxidation of supported iron (2% Fe/Al_2O_3) was faster

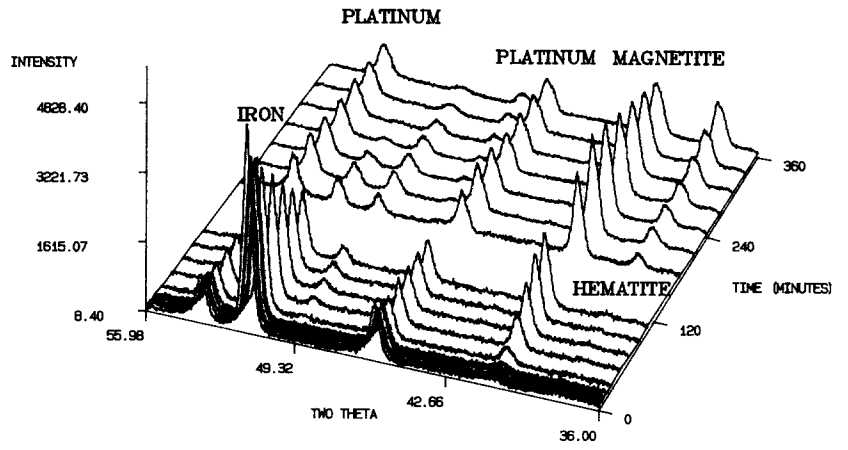

FIG. 9. DXRD oxidation data for unsupported iron (T = 673 K, P_{CO_2} = 100 kPa).

than that of bulk Fe powder. They attributed this observation to the small size of supported iron particles. The same is true here (Table 1), and this plays a major role in the large difference in the oxidation rates between the supported iron and the unsupported iron. However, Berry *et al.* (*36*) showed that iron–ruthenium supported on alumina and on silica have different oxidation behaviors at room temperature, which suggests that support interactions can also result in different oxidation kinetics. More recently, Burkhardt and Schmidt (*37*) have also observed lower oxidation temperatures with Rh and Ir supported on alumina as opposed to the same metals supported on silica. Thus it appears that alumina supports enhance oxidation rates to a certain degree.

The fact that the oxidation rate of the supported iron catalyst is higher than that of the unsupported iron can be attributed to two factors: its smaller sized iron particles and the consequence of metal–support interactions. The evidence for the latter lies in the DXRD observations which clearly show that the iron particles with high aluminum concentrations oxidize at a faster rate than those with lower concentrations. This result is also supported by the theory that, for *p*-type oxides, the dissolution of higher valence cations such as Al_2O_3, leads to the creation of more cation vacancies and a reduction of the electron hole concentration, thus increasing cation conductivity and decreasing electron conductivity. The net effect is to increase the oxidation rate (*34*).

In a comparison of the reduction kinetics (Fig. 8) with the oxidation kinetic data shown in Fig. 10, it is apparent that the rate determining steps are different. While reduction clearly followed an interface reaction controlled mechanism, oxidation resulted in linear kinetics. The latter can be expected early in diffusion controlled oxidation when the oxide layer is thin. However, since the particle sizes here are so small, diffusion control is not likely. Thus it appears that the oxidation rate of the supported iron ($(1\text{-}R) < 0.89$) is governed by either the adsorption of CO_2 or its subsequent dissociation (*34*), both of which yield linear kinetics.

As mentioned above, the final oxidation state of the supported iron catalyst was γ-Fe_2O_3 (maghemite) whereas unsupported iron oxidized to α-Fe_2O_3 (hematite) at 673 K. The reason that γ-Fe_2O_3 is formed during oxidation of the supported iron is strongly believed to be due to impurities in the iron which, in this case, are aluminum ions. It is known that the γ-Fe_2O_3 spinel lattice is thermodynamically stabilized by reticular

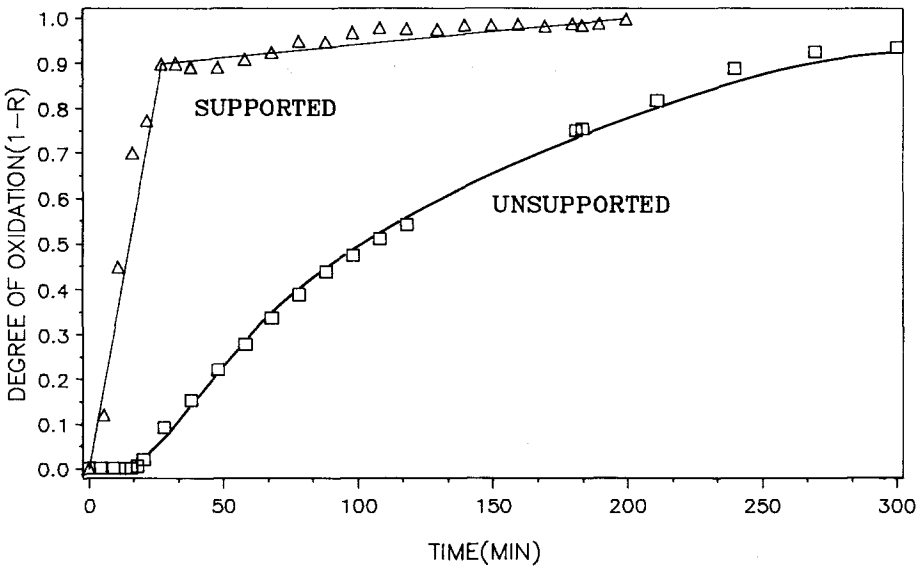

FIG. 10. Iron oxidation rates (T = 673 K, P_{CO_2} = 100 kPa).

impurities and by other crystalline imperfections (*38*). Formation of γ-Fe_2O_3 occurs through a topotactic transformation of Fe_3O_4 spinel which is characterized by internal atomic displacement (even with the losses or gains of material), so that there is accord in three dimensions between the initial and final lattices (*39*). On the other hand, α-Fe_2O_3 forms from magnetite by epitaxial growth. The results here are again consistent with those of Boudart *et al.*'s work with a Fe/MgO catalyst (*28*). After observing an FeO–MgO solid solution during reduction, they also found that the oxidized form of the catalyst was γ-Fe_2O_3. It is also known that the transition temperature of γ-Fe_2O_3 to α-Fe_2O_3 rises by about 350 K when 7% of Fe^{3+} is replaced by Al^{3+} (*40*). Similar behavior was observed here in that the supported γ-Fe_2O_3 was converted to α-Fe_2O_3 at temperatures higher than 873 K. Thus all of the reduction and oxidation results are compatible with the conclusion that aluminum is incorporated in the supported iron oxide particle. The incorporated Al in the matrix of the supported magnetite may explain its lower WGS activity as compared to the promoted catalyst in which the chromia functions as a textural promoter (*41*).

CONCLUSIONS

As discussed above, all of the data with the supported iron catalyst are consistent with the occurrence of interactions between the iron and the support. The fact that there are lattice parameter shifts in the fresh calcined catalyst is an indication of the incorporation of Al into the supported iron particles. Not only is this substantiated by the slow reduction rate of the supported iron oxide, but the behavior of XRD patterns during reduction points to the fact that the Al is unevenly distributed in the iron oxide. The latter results in two distinct reduction rates when rate data are analyzed by conventional interface reaction controlled kinetic models. Finally, the subsequent oxidation of the reduced iron also confirms the existence of interactions with the support; the oxidation rates of the supported iron are much higher than those measured with the unsupported iron, and the specific phase of Fe_2O_3 which is formed at these temperatures in the sup-

ported catalyst is γ-Fe_2O_3, a phase which is known to form when impurities are incorporated into the iron structure. Thus, even though the iron particle sizes in the supported catalyst are much smaller than in the unsupported samples, the fact that the reduction rates are slower and a different oxidation product is produced in the former is strong evidence that the interaction between the iron and the support is the primary factor here.

ACKNOWLEDGMENTS

This material is based upon work supported by the National Science Foundation under Grant CBT-8719929. The government has certain rights in this material.

REFERENCES

1. Pernicone, N., and Traina, F., *Pure Appl. Chem.* **50,** 1169 (1978).
2. Pattek, A., and Hrynkiewicz, A. Z., *Appl. Catal.* **6,** 27 (1983).
3. Pattek, A., Hrynkiewicz, A. J., Kraczka, J., and Kulgawczuk, D., *Appl. Cata.* **6,** 35 (1983).
4. Baranski, A., Bielanski, A., and Pattek, A., *J. Catal.* **26,** 286 (1972).
5. Pernicone, N., Liberti, G., and Servi, G., *Prog. Vac. Microbalance Tech.* **3,** 304 (1975).
6. Topsøe, H., Dumesic, J. A., and Boudart, M., *J. Catal.*, **28,** 477 (1973).
7. Fagherazzi, G., Galante, F., Garbassi, F., and Pernicone, N., *J. Catal.* **26,** 344 (1972).
8. McKewan, W. M., *Trans. Amer. Inst. Min. Metall. Pet. Eng.* **218,** 1 (1960).
9. Spitzer, R. H., Manning, F. S., and Philbrook, W. O., *Trans. Amer. Inst. Min. Metall. Pet. Eng.* **236,** 726 (1966).
10. Colombo, U., Gazzarrini, F., and Lanzavecchia, G., *Mater. Sci. Eng.* **2,** 125 (1967).
11. Themelis, N. J., and Gauvin, W. H., *Trans. Amer. Inst. Min. Metall. Pet. Eng.* **227,** 290 (1963).
12. Holm, C. F., and Clark, A., *J. Catal.* **11,** 305 (1968).
13. Garten, R. L., and Ollis, D. F., *J. Catal.* **35,** 232 (1974).
14. Stevenson, S. A., Raupp, G. B., Dumesic, J. A., Tauster, S. J., and Baker, R. T. K., *in* "Metal–Support Interactions in Catalysis, Sintering and Redispersion"(S. A. Stevenson, J. A. Dumesic, R. T. K. Baker, and E. Ruckenstein, Eds.), p. 7. Van Nostrand–Reinhold, New York, 1987.
15. Tang, R., Zhang, S., Wang, C., Liang, D., and Lin, L., *J. Catal.* **106,** 440 (1987).
16. Sushumna, I., and Ruckenstein, E., *J. Catal.* **106,** 440 (1987).
17. Hobson, M. C., and Gager, H. M., *J. Catal.* **16,** 254 (1970).
18. Cullity, B. D., "Elements of X-Ray Diffraction." Addison–Wesley, Reading, MA, 1978.
19. Nix, R. M., Rayment, T., Lambert, R. M., Jennings, J. R., and Owen, G., *J. Catal.* **106,** 216 (1987).
20. Walker, A. P., Rayment, T., and Lambert, R. M., *J. Catal.* **117,** 102 (1989).
21. Anderson, D. E., and Thomson, W. J., *Ind. Eng. Chem. Res.* **26,** 1628 (1987).
22. Thomson, W. J., *Ceram. Trans.* **5,** 131 (1989).
23. Anderson, D. E., Ph.D. thesis, Washington State University, Pullman, 1988.
24. Klug, H. P., and Alexander, L. E., "X-Ray Diffraction Procedures: For Polycrystalline and Amorphous Materials," 2nd ed. Wiley, New York, 1974.
25. Rooksby, H. D., "The X-Ray Identification and Crystal Structures of Clay Materials." Mineralogical Society, London, 1961.
26. Vaishnava, P. P., Ktorides, P. I., Montano, P. A., Mbadcam, K. J., and Melson, G. A., *J. Catal.* **96,** 301 (1985).
27. Garbassi, F., Fagherazzi, G., and Calcaterra, M., *J. Catal.* **26,** 338 (1972).
28. Boudart, M., Delbouille, A., Dumesic, J. A., Khammouma, S., and Topsøe, H., *J. Catal.* **37,** 486 (1975).
29. Lund, C. R. F., and Dumesic, J. A., *J. Catal.* **72,** 21 (1981).
30. Lo Jacono, M., Schiavello, M., and Cimino, A., *J. Phys. Chem.* **75,** 1044 (1971).
31. Dufrense, P., Payen, E., Grimblot, J., and Bonnelle, J. P., *J. Phys. Chem.* **85,** 2344 (1981).
32. Shalvoy, R. B., Reucroft, P. J., and Davis, B. H., *J. Catal.* **56,** 336 (1979).
33. Turkdogan, E. T., and Vinters, J. V., *Metall. Trans.* **2,** 3275 (1971).
34. Birks, N., and Meier, G. H., "Introduction to High Temperature Oxidation of Metals." Edward Arnold, London, 1984.
35. Kadkhodayan, A., and Brenner, A., *J. Catal.* **117,** 311 (1989).
36. Berry, F. J., Lin, L., Wang, C., Tag, R., Zhang, S., and Liang, D., *J. Chem. Soc. Faraday Trans. I* **81,** 2293 (1985).
37. Burkhardt, J., and Schmidt, L. D., *J. Catal.* **116,** 240 (1989).
38. Colombo, U., Fagherazzi, G., Gazzarrini, F., Lanzavecchia, G., and Sironi, G., *Nature (London)* **202,** 175 (1964).
39. Colombo, U., Gazzarrini, F., Lanzavecchia, G., and Sironi, G., *Science* **147,** 1033 (1965).
40. Basta, E. Z., *Econ. Geol.* **54,** 698 (1959).
41. Salmi, T., Lindfors, L.-E., and Bostrom, S., *Chem. Eng. Sci.* **41,** 929 (1986).